Self-assembling endohedrally doped CdS nanoclusters: new porous solid phases of CdS

Elisa Jimenez-Izal,*[a] Jon M. Matxain,[a] Mario Piris[a,b] and Jesus M. Ugalde[a]

[a] *Kimika Fakultatea, Euskal Herriko Unibertsitatea and Donostia International Physics Center (DIPC), P.K. 1072 Donostia, Euskadi, Spain.*
[b] *IKERBASQUE, Basque Foundation for Science, 48011 Bilbao, Spain*

Corresponding author E-mail: elisa.jimenez@ehu.es

Abstract

Hollow CdS nanoclusters were predicted to trap alkali metals and halogen atoms inside their cavity. Furthermore, electron affinities (EA) of endohedrally halogen doped clusters and ionization potentials (IE) of endohedrally alkali doped clusters were predicted to be very similar. This makes them suitable to build cluster-assembled materials, in the same vein as do related ZnO, ZnS and MgO nanoclusters, which yield porous solid materials. With this aim in mind, we have focused on the assembly of bare Cd_iS_i and endohedral $K@Cd_iS_i$–$X@Cd_iS_i$ (i = 12, 16, X = Cl, Br) clusters in order to obtain solids with tailored semiconducting and structural properties. Since these hollow nanoclusters possess square and hexagonal faces, three different orientations have to be considered, namely, edge-to-edge (E–E), square-to-square (S–S) and hexagon-to-hexagon (H–H). These three orientations lead to distinct zeolite-like nanoporous bulk CdS solid phases denoted as SOD, LTA and FAU. These solids are low-density crystalline nanoporous materials that might be useful in a wide range of applications ranging from molecular sieves for heterogeneous catalysis to gas storage templates.

1 Introduction

Novel classes of solid materials with nanoclusters as building blocks 1 can be nowadays synthesized due to recent experimental advances that allow the production of nanoclusters of a given size and composition. 2 This fact has developed a new research concept that consists of the fabrication of nanocluster-assembled materials. The success of this assembling depends on the capability of the nanoclusters to retain their structure in the assembled material. In this vein, it is notable that the less prone to collapse nanoclusters are those with closed electronic shells. Fullerite crystals, 3,4 made of hollow spherical C_{60} structures, are a good example.

Consequently, hollow (pseudo) spherical nanoclusters are receiving much attention, not only because of their resemblance to C_{60}, but also because they can trap atoms and molecules inside their cavity and thus offer a new way of controlling the properties of the resulting

nanoclusters by endohedral doping. The first such endohedrally doped cluster was La@C_{60}, which was discovered by Heath et al. in 1985; 5 since then many other carbon fullerene endohedral clusters have been characterized. 6–8 Endohedral hollow clusters of elemental metals, such as M@Au_n cages, 9–12 endohedrally doped plumbaspherene TM@Pb_{12} cages, 13 and endohedrally doped stannaspherene TM@Sn_{12} cages, which have been seen to exist in the gas phase for a large number of transition metals (TMs), 14 have also been synthesized. Additionally, neutral Mn@Sn_{12} endohedral compounds have been predicted to be stable enough to allow the formation of its corresponding dimer, which yields an antiferromagnetic coupling of the two Mn^{2+} quintet endohedral cations. 15

Binary hollow nanoclusters of semiconductor elements, such as Group II–VI elements, have also been investigated. 16–26 Likewise, the assembly of this kind of cluster has been studied in the last few years. For instance, Carrasco et al. predicted new low-density solid phases via assembling $(MO)_{12}$ clusters (M = Mg, Zn). 27 These structures resemble that of LTA, FAU and SOD zeolites, following the framework notation of the corresponding silicate topologies. 28 Furthermore, Woodley and co-workers constructed cubic nano- and microporous ZnO frameworks from octahedral bubble clusters. The frameworks were constructed by arranging the clusters so that octahedra were corner sharing, and, in some cases, with ordered vacancies. 29 They also considered more dense frameworks of edge and face sharing octahedra. Additionally, Wang et al. found using first-principles calculations a metastable solid-phase soldalite structure via coalescence of $(ZnO)_{12}$ cages. 30 Zwijnenburg and co-workers showed that for MX compounds (AgI, ZnO, ZnS, CdS, GaN, GaP and SiC) there exists a dense spectrum of as yet undiscovered polymorphs, the majority of which lie only moderately higher in energy than the experimentally observed phases. 31 Moreover, they explored the chemical and structural analogy between nanoporous zeolites and co-substituted binary MX materials (primarily on ZnO derived compounds), finding numerous low-energy structures. 32 In addition to this, a theoretical study of the assembly of $M_{12}N_{12}$ (M = Al, Ga) nanoclusters by either square or hexagonal faces, giving rise to cubic or rhombohedral nanoporous phases, was reported by Yong and co-workers. They found both phases to be wide-gap semiconductors, the rhombohedral one being energetically more favorable. 33 In a later work, they investigated $Zn_{12}O_{12}$ assembled material by attaching a $Zn_{12}O_{12}$ cage on a hexagonal face, which brings about a new three dimensional ZnO phase with a rhombohedral lattice framework. 34 Finally, the 1-D condensed clusters $(Cd_nS_n)_m$, where n = 1–4 and m = 1–9, were modeled and it was observed that $(Cd_3S_3)_m$ frameworks are energetically more stable as compared with other-sized condensed clusters.

In this vein, the use of endohedral compounds made of these hollow semiconducting nanoclusters as building blocks broadens the horizon of possibilities of obtaining new solids with desired properties. In previous works we hypothesized the existence of endohedrally doped, both neutral and charged, X@Zn_iS_i compounds (i = 4–16; X = Cl, Br, Na, K), 35 and that these X@$Zn_{12}S_{12}$ compounds could form metastable fcc-like cluster-assembled solids. 36 These structures resemble that of LTA zeolites, where the clusters were linked together by their squares. The so formed nanoporous solids were metastable, having band-gaps decreased with respect to their corresponding most stable bulk solid phases by the effect of doping.

In this work we have dealt with the assembly of previously characterized $X@Cd_iS_i$, i = 12,16 nanoclusters. 37 These clusters were chosen due to their high stability and high symmetry, which ensures that (i) the stability of the cluster structures themselves is not compromised by the endohedral doping and (ii) a larger variety of properties can be tailored by such doping. Consequently, one could think of using these bare and doped nanoclusters as building blocks to synthesize stable solids, in the same vein as the other related solids mentioned previously. Specifically, we have considered CdS nanoclusters doped with alkali metals and halogens: $K@Cd_iS_i$–$X@Cd_iS_i$ (i = 12, 16, X = Cl, Br). It should be pointed out that the electron affinities of halogen doped clusters and the ionization potential of the alkali doped clusters are very similar, and even higher than the EA and IP of the corresponding halogen and alkali atoms. 37 Indeed, the encapsulated potassium atom donates an electron to the cage, while the encapsulated halogen atom removes an electron from the cage, which leads to clusters with ions inside the cage. This makes them suitable to form ionic-cluster-assembled materials, in a similar way to the $X@Zn_{12}S_{12}$–$Y@Zn_{12}S_{12}$ (X = Na, K; Y = Cl, Br) case, studied earlier by Matxain and co-workers. 36 The assembling modes considered in this work are the ones resembling the three zeolites mentioned above, FAU, SOD and LTA. The structures of the nanoclusters make possible, since they are composed of squares and hexagons, three different orientations forming the three zeolite-like nanoporous bulk CdS phases: hexagon to hexagon (H–H), square to square (S–S) and edge to edge (E–E), which are related to the FAU, LTA and SOD structures, respectively. First, the dimers formed in such ways have been studied, and then these dimer structures are taken as unit cells for the calculations of the proposed solids.

2 Methods

To calculate the interaction energies for the cluster dimers, bare cluster monomer geometries 24 and doped monomer geometries 37 were used. These geometries were fully optimized by the gradient-corrected hybrid B3LYP 38–40 functional within the Kohn–Sham implementation 41 of density functional theory. 42 Harmonic vibrational frequencies were calculated by analytical differentiation of gradients to determine whether the structures found are true minima and to extract zero-point and thermal corrections for the energies. The relativistic compact effective core potentials and the shared-exponent basis set of Stevens et al. (SKBJ) 43 were used for Zn and S as described in the study of the isolated clusters, 24 and the all-electron 6-311+G(d) basis set for the trapped atoms. Notice that pure angular momentum functions were used throughout this study. All geometry optimizations and frequency calculations were carried out by using the Gaussian 09 package. 44 All the atomic charges are calculated from the trace of the atomic polar tensor.

Molecular solids composed of both bare and endohedrally doped $Cd_{12}S_{12}$ and $Cd_{16}S_{16}$ clusters were explored by DFT calculations performed by using the SIESTA computer code. 45 Exchange and correlation effects were described by using the generalized gradient approximation (GGA), within the revised Perdew–Burke–Ernzerhof (rPBE) functional. 46,47 Core electrons were replaced by Troullier–Martins norm-conserving pseudopotentials 48 in the Kleinman–Bylander factorized form. 49 The use of pseudopotentials, as implemented in

SIESTA, imposes basis set orbitals adapted to them. Furthermore, SIESTA employs a localized basis set to represent the Kohn–Sham orbitals for valence electrons. Accordingly, the basis set of atomic orbitals is constructed from numerical solutions of the atomic pseudopotential, and is constrained to be zero beyond a cutoff radius. We chose a basis set of double-z plus polarization (DZP) quality. The single parameter (orbital energy shift) that defines the confinement radii of different orbitals was DE_{PAO} = 50 meV, which gives a rather good precision within the accuracy of the GGA functional used. With this basis set, SIESTA calculates the self-consistent potential on a grid in real space. The fineness of this grid is determined in terms of an energy cutoff, in analogy to the energy cutoff when the basis set involves plane waves. In our calculations, we used an equivalent plane wave cutoff energy of 300 Ry. In all cases, the geometry was relaxed until the maximum forces were smaller than 0.04 eV/Å. For the solid-state calculations, we have used 18 K points. Both the intra- and intercell parameters have been optimized. The combination of these two methodologies, one for dimers and another one for Solids have been previously proven to be reliable. 36,50

3 Results

The unit cells of the characterized solids are chosen to be the dimers of the nanoclusters, to ensure the formation of the favourable Cd–S interactions between nanoclusters, in opposition to less favourable Cd–Cd or S–S interactions. Thus, first of all we have characterized the dimers: Cd_iS_i and $K@Cd_iS_i$–$X@Cd_iS_i$ (i = 12, 16, X = Cl, Br). Then, the solids have been constructed by using the optimum dimer structures as starting geometries for the unit cells.

In Section 3.1 the optimized structures, calculated interaction energies, charges and HOMO–LUMO gaps of both bare and endohedrally doped dimers are discussed. Next, in Section 3.2, we will focus on the properties of the characterized solids, including band gaps and cohesive energies.

3.1 Dimers

The lowest-energy minimum for the isolated $Cd_{12}S_{12}$ cluster was found to be composed of eight hexagons and six squares, having T h symmetry. 24,25 On the other hand, the lowest-energy minimum for $Cd_{16}S_{16}$ is composed of twelve hexagons and six squares and its point group is T_d. 24,25 This structural pattern and symmetry is not altered after endohedral doping. 37 Therefore, these structures have been chosen as the basis to build up the dimers under study. As these clusters are composed of hexagons and squares, they can be linked together in three different ways: (i) by bonding monomers via hexagonal faces, (ii) square–square interfacial bonding, (iii) via edge to edge interactions. The resulting dimers are shown in Fig. 1 for $K@Cd_iS_i$–$Br@Cd_iS_i$. The symmetry group corresponding to each case is given in Table 1. All bare dimers are highly symmetrical. However, in several of the doped dimers the symmetry is broken due to the fact that the electrostatic interactions force the caged ions to move out the center of the nanoclusters. Nevertheless, the main structural patterns of the monomers are unaffected by dimerization, proving the high stability of $Cd_{12}S_{12}$ and $Cd_{16}S_{16}$ nanoclusters which, henceforth, makes them suitable candidates for assembling into solids.

In Table 1 the charges of potassium and halogen atoms, the dimerization energies and the HOMO–LUMO energy gaps are shown. The distance between the encapsulated potassium and halogen atoms, R, has been measured to characterize the optimum geometry of the dimers and is also given in Table 1. In the case of bare dimers, R is the distance between the center of mass of the two monomers. Observe that, in bare dimers, as the number of covalent bonds between the monomers decreases from H–H dimers to E–E ones, R increases, as expected. Additionally, after doping, R decreases even more due to the long range electrostatic interaction between the encapsulated K and halogen atoms. This fact is reflected in the charges of guest atoms. To explain it, we have to take into account that the ionization potentials of potassium doped nanoclusters and the electron affinities of halogen doped ones are very similar. 37 Consequently, this leads to a formal charge transfer from the potassium to the halogen, resulting in a cation and an anion trapped in two hollow neutral Cd_iS_i clusters. Notice that this decrease of R after doping is larger in the H–H and S–S cases (B1 Å) than in the E–E case (B0.5 Å). H–H and S–S dimers form an ‘‘empty’’ zone in the line connecting the trapped atoms, while the E–E dimers have intra-cluster covalent bonds, just on this line, which repel the trapped atoms and prevent them from moving closer.

The dimerization energies were calculated with respect to the isolated neutral components of each dimer, in both bare and doped cases. All the dimers have negative dimerization energies. This means that all of them are predicted to be thermodynamically stable. In all bare and doped dimers, there is a trend in the stability: the stability decreases from dimers linked by hexagons to dimers linked by edges. Namely, the stability decreases when the number of bonds between monomers decreases too. Comparing the dimerization energies of $Cd_{12}S_{12}$ and $Cd_{16}S_{16}$ reveals that they are very similar. So, we can conclude that size is not a determinant factor for thermodynamic stability. Finally, it must be highlighted that the overall stability increases after doping.

When analyzing the HOMO–LUMO gaps, we have kept in mind that DFT tends to underestimate these values. However, inspection of the HOMO–LUMO gaps shown in Table 1 clearly shows that endohedral doping significantly reduces the gap. The largest decrease takes place for the E–E dimers (1–1.5 eV), while the lowest decrease occurs for the H–H dimers (B0.6 eV). The dopant effect is also larger for the $Cd_{12}S_{12}$ compounds. This effect is very similar for different halogen dopants; Cl and Br have similar effects.

3.2 Solids

In this subsection the properties of the characterized bare Cd_iS_i–Cd_iS_i and doped K@Cd_iS_i–X@Cd_iS_i (i = 12, 16, X = Cl, Br) solids are discussed. These solids have been characterized by using the optimum dimer structures as starting geometries for the unit cells. As these clusters are composed of hexagons and squares, they can be assembled in different ways, H–H, S–S and E–E. Thus, we have constructed three new crystalline phases of CdS to form zeolite like nanoporous bulk phases which are depicted in Fig. 2: (i) FAU-CdS (based on H–H dimers), (ii) LTA-CdS (based on S–S dimers) and (iii) SOD-CdS (based on E–E dimers).

In Table 2 the lattice parameters (a, b and c), the distance between the encapsulated atoms (R) and the volume of the unit cell [V ($Å^3$)] are given along with the cohesive energies [E_{coh} (eV)] and the band gaps calculated at G points [DG (eV)] of the characterized solids. For the calculation of the cohesive energy, the following thermodynamic cycle has been used:

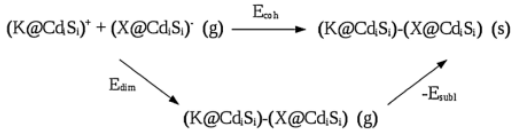

Thus, the cohesive energy is calculated as the sum of the dimerization energy minus the sublimation energy. Notice that in calculating wurtzite cohesive energy, 4 Cd–S bonds are broken per atom, while in all SOD, LTA and FAU structures, 24 Cd–S bonds are broken to yield isolated nanoclusters. Therefore, the ratio is 1/6. So, for the cohesive energies of our structures to be comparable with the cohesive energy corresponding to bulk CdS wurtzite, the obtained values must be divided by six.

Looking at the cohesive energies given in Table 2, it can be observed that, after doping, all solids become thermodynamically more stable, increasing their cohesive energies with respect to their corresponding bare structures. This stabilization due to the doping is also observed in the dimers. However, in the latter the less stable structure (dimers linked by edges) becomes in solid phase the most stable and vice-versa. To rationalize this fact, the reader has to take into consideration an important factor present in the solid structure and not in the dimer: the compactness. The unit cell volume provides an illustration. In the case of solids made of $Cd_{12}S_{12}$, the FAU phase is the less compact structure (the largest volume), while SOD is the most compact one (smaller volume). In the case of $Cd_{16}S_{16}$, the order is slightly different: the LTA phase is the less compact structure (the largest volume), and SOD is the most compact one (smaller volume). Note that, in contrast to $Cd_{12}S_{12}$ solid phases, in all the $Cd_{16}S_{16}$ solid phases there are square–square contacts due to the symmetry of the monomer.

In conclusion, in all cases the SOD phase has the largest cohesive energy, being the thermodynamically most stable solid. In fact, the cohesive energy of CdS in the zinc blende structure is 2.44 eV; 51 similar to that are SOD doped phases. In addition, it should be noted that the SOD structure has the smallest pores, which is directly linked to the cell volume. Lattice parameters for all calculated solids are shown in Table 2. Note that the more compact the structure is, the smaller these parameters are, as expected, and that doping does not affect them significantly. These cell parameters correspond to bond lengths of around 2.7 Å between cells, which indicates covalent CdS bonds between cells. In the case of LTA and FAU $Cd_{12}S_{12}$ solids, each potassium atom is surrounded by halogens and vice-versa. This yields more spherical cluster moieties in the solids than in the dimers, due to the neighbours' effects (in all directions in the solid and in only one in the dimer). Concomitantly, in these solids the dopant ions sit at the center of their corresponding clusters, hence R values for the solids match with the distances between the center of mass of two adjacent clusters, in contrast to the dimers.

However, in the case of the SOD $Cd_{12}S_{12}$ phase, each cation is surrounded by anions in 2 directions while the third direction has cations too on each side and vice-versa. The same happens in the FAU $Cd_{16}S_{16}$ structure. Finally, in SOD and LTA $Cd_{16}S_{16}$ phases, cations are surrounded by anions only in one direction, having other cations in the other two. Consequently, the guest atoms are not in the centers of the nanoclusters, but close to them. For these cases, R values shown in Table 2 are calculated as the average of all the distances between each potassium and the closest halogens.

The analysis of the band gaps at the G point shows that our calculations predict all the solids to be semiconductors. Moreover, the band-gaps greatly decrease when doping the solids. This can be understood by looking at Fig. 3, LTA-$Cd_{12}S_{12}$, LTA-K@Cd_iS_i–Cl@$Cd_{12}S_{12}$ and LTA-K@Cd_iS_i–Br@$Cd_{12}S$ phases are plotted respectively. Observe that some of the dopants occupy bands which are located between the valence and the conducting bands. In all cases, SOD structure is the phase with the smallest band-gap because it has the most compact crystalline structure. This fact is specially marked for SOD-K@$Cd_{16}S_{16}$–Cl@$Cd_{16}S_{16}$, for which the band-gap is almost zero. As found earlier, 24,36 the valence band of the bare solid is made mainly by the 3p atomic orbitals of the sulfur atoms and the largest contribution to the conduction band comes from the 5s orbitals of the cadmium atoms. Moreover, the bandwidths of the conduction bands of the doped solids (0.6 eV) are similar to that of the bare solid and they also come from the 5s atomic orbitals of the Cd atoms. However, the valence band of the doped solid arises from the valence atomic orbitals of the encapsulated halogen atoms, which nearly interact with the 5s orbitals of the cadmium atoms. This results in substantially decreased band-widths for the doped solids and a concomitant reduction in the band gap.

Finally, it should be pointed out that the characterized structures in this work are not the most stable phases of CdS. These structures are much less dense than the more stable structures found in nature, namely wurtzite and zinc blende, in fact, these new phases reported here can be regarded as metastable phases of CdS. This can be seen looking at Fig. 4, where the cohesive energies of the characterized solids are depicted as a function of cell volume. Note that in these structures we have set the same number of atoms in the unit cell for each plot, so the calculations with wurtzite have been carried out on an extended unit cell. For the sake of brevity, we have plotted only bare structures.

For $Cd_{12}S_{12}$, the SOD phase is predicted to be almost as stable as wurtzite, but at larger unit cell volume, or, equivalently, under lower pressure conditions. It is very interesting to relate once again the compactness (volume) of these phases with their thermodynamic stability. As seen in Table 2, the most compact phase is the most stable one. In this vein, wurtzite is the most compact solid, followed by SOD, LTA and FAU phases for $Cd_{12}S_{12}$ compounds. Nonetheless it is worth mentioning that the energy difference between wurtzite and SOD is only 0.66 eV, while the difference between wurtzite and FAU is 4.74 eV.

In the case of $Cd_{16}S_{16}$, we found that the new phases characterized in this work are predicted to be metastable too. Likewise, the order in the stability is now slightly different, LTA being the least stable phase. However, it is clear from Fig. 4 that the energy differences are much larger

with respect to wurtzite (wurtzite SOD = 6.35 eV; wurtzite LTA = 9.43 eV). One reason for this may be the symmetry of the monomer: as mentioned before, differently to $Cd_{12}S_{12}$-build phases, in all the $Cd_{16}S_{16}$-build solids there are square–square contacts which turn out to decrease the cohesive energies with respect to the wurtzite structures.

It is also remarkable the fact that while there is a clear energy barrier for the transition between wurtzite and SOD phases, it seems that there is not any energetic barrier between LTA and FAU phases. Consequently, the FAU-$Cd_{12}S_{12}$ phase would spontaneously transform into LTA-$Cd_{12}S_{12}$ and LTA-$Cd_{16}S_{16}$ into FAU-$Cd_{16}S_{16}$.

4 Conclusions

We have shown that the Cd_iS_i nanoclusters, for i = 12, 16, form stable bare and endohedrally doped nanocluster dimers doped with K and halogens such as Cl and Br. As the ionization potential of K doped monomers and the electron affinities of halogen doped ones are very similar; there is a charge transfer from the potassium to the halogen that can be seen as a cation and an anion trapped in two hollow neutral clusters. These dimers can be different according to the contact zone: hexagons to hexagons (H–H), squares to squares (S–S) and edges to edges (E–E), where the monomers are linked together by covalent bonds between Zn and S. In all the dimers the electronic and structural integrity of bare nanoclusters are completely retained. We have observed that their stability decreases when the number of bonds between monomers decreases too (H–H being the most stable dimer) and that the size of the cluster does not affect the stability. It must be highlighted that the stability increases and the HOMO–LUMO gaps are reduced after doping.

Additionally, the characterized dimers were further used as starting geometries of the unit cells in solid-state calculations. Hence, we have constructed three new crystalline phases of CdS to form zeolite like nanoporous bulk phases: (i) FAU-CdS (based on H–H dimers), (ii) LTA-CdS (based on S–S dimers) and (iii) SOD-CdS (based on E–E dimers). The analysis of the band gaps at the G point shows that all the solids are predicted to be semiconductors. Moreover, endohedral doping decreases the band gaps by 0.4 eV, that is, from 2.2 eV in the bare solid to 1.8 eV in the doped solids. Therefore, these solids may be seen as narrow-gap semiconducting materials. Besides, all the solids have been found to be thermodynamically stable with cohesive energies similar to many soft solids. Furthermore, endohedral doping increases their stability. However, the characterized structures in this work are not the most stable phases of CdS. These structures are much less dense than the most stable structures found in nature, namely wurtzite and zinc blende, indeed, these new phases can be regarded as metastable phases of CdS. As a matter of fact, the SOD phase is the most stable solid of all the characterized ones, due to its high compactness.

Thus, we conclude that it should be possible to stabilize new nanoporous polymorphic solid phases of CdS, with much larger unit cells as compared with the solid phases found in nature. Indeed, the solids characterized in this work are less compact than wurtzite and zinc blende. This fact has two important consequences: it makes these new materials thermodynamically

metastable. Conversely, they might have many applications, due to their large pores, in heterogeneous catalysis and as storage materials.

Acknowledgements

Financial support comes from Eusko Jaurlaritza and the Spanish Office Scientific Research. The SGI/IZO-SGIker UPV/EHU is gratefully acknowledged for generous allocation of computational resources. JMM would like to thank the Spanish Ministry of Science and Innovation for funding through a Ramon y Cajal fellow position (RYC 2008-03216). EJ-I would like to thank the Basque Government for a doctoral grant.

References

1 S. N. Khanna, B. K. Rao and P. Jena, Phys. Rev. Lett., 2002, 89, 16803.
2 P. Jena and A. W. Castleman, Proc. Natl. Acad. Sci. U. S. A., 2006, 103, 10560.
3 M. R. Pederson and A. A. Quong, Phys. Rev. Lett., 1995, 74, 2319.
4 B. L. Zhang, C. Z. Wang, K. M. Ho and C. T. Chan, Europhys. Lett., 1994, 28, 219.
5 J. R. Heath, S. C. O'Brien, Q. Zheng, Y. Liu, R. F. Curl, H. W. Kroto, F. K. Tittel and R. E. Smalley, J. Am. Chem. Soc., 1985, 107, 7779.
6 S. Erkoc and L. Turker, THEOCHEM, 2003, 634, 195.
7 M. S. Dresselhaus, G. Dresselhaus and P. C. Eklund, Science of fullerenes and carbon nanotubes, Academic Press, San Diego, 1996.
8 C. M. Cardona, B. Elliott and L. Echegoyen, J. Am. Chem. Soc., 2006, 128, 6480.
9 P. Pyykko and N. Runeberg, Angew. Chem., Int. Ed., 2002, 41, 2174.
10 X. Li, B. Kiran, J. Li, H. J. Zhai and L. S. Wang, Angew. Chem., Int. Ed., 2002, 41, 4786.
11 H. J. Zhai, J. Li and L. S. Wang, J. Chem. Phys., 2004, 121, 8369.
12 L. M. Wang, S. Bulusu, H. J. Zhai, X. C. Zeng and L. S. Wang, Angew. Chem., Int. Ed., 2007, 46, 2915.
13 X. Chen, K. Deng, Y. Liu, C. Tang, Y. Yuan, F. Hu, H. Wu, D. Huang, W. Tan and X. Wang, Chem. Phys. Lett., 2008, 462, 275.
14 L. Cui, X. Huang, L. Wang, J. Li and L. Wang, Angew. Chem., Int. Ed., 2007, 46, 742.
15 J. M. Matxain, M. Piris, E. Formoso, J. M. Mercero, X. Lopez and J. M. Ugalde, ChemPhysChem, 2007, 8, 2096.
16 S. Hamad, S. Cristol and C. R. A. Catlow, J. Am. Chem. Soc., 2005, 127, 9479.
17 S. Hamad, C. R. A. Catlow, E. Spano, J. M. Matxain and J. M. Ugalde, J. Phys. Chem. B, 2005, 109, 2703.
18 J. M. Matxain, J. E. Fowler and J. M. Ugalde, Phys. Rev. A, 2000, 61, 53201.
19 J. M. Matxain, J. E. Fowler and J. M. Ugalde, Phys. Rev. A, 2000, 62, 53201.
20 J. M. Matxain, A. Irigoras, J. E. Fowler and J. M. Ugalde, Phys. Rev. A, 2001, 63, 13202.
21 J. M. Matxain, A. Irigoras, J. E. Fowler and J. M. Ugalde, Phys. Rev. A, 2001, 64, 13201.
22 J. M. Matxain, J. M. Mercero, J. E. Fowler and J. M. Ugalde, Phys. Rev. A, 2001, 64, 53201.
23 J. M. Matxain, J. M. Mercero, J. E. Fowler and J. M. Ugalde, J. Am. Chem. Soc., 2003, 125, 9494.

24 J. M. Matxain, J. M. Mercero, J. E. Fowler and J. M. Ugalde, J. Phys. Chem. A, 2004, 108, 10502.
25 A. Burnin, E. Sanville and J. J. BelBruno, J. Phys. Chem. A, 2005, 109, 5026.
26 E. Sanville, A. Burnin and J. J. BelBruno, J. Phys. Chem. A, 2006, 110, 2378.
27 J. Carrasco, F. Illas and S. T. Bromley, Phys. Rev. Lett., 2007, 99, 235502.
28 Handbook of Zeolite Science and Technology, ed. S. M. Auerbach, K. A. Carrado and P. K. Dutta, Marcel Dekker, New York, 2003.
29 S. M. Woodley, M. B. Watkins, A. A. Sokol, S. A. Shevlin and C. R. A. Catlow, Phys. Chem. Chem. Phys., 2009, 11, 3176.
30 B. Wang, X. Wang and J. Zhao, J. Phys. Chem. C, 2010, 114, 5741.
31 M. A. Zwijnenburg, F. Illas and S. T. Bromley, Phys. Rev. Lett., 2010, 104, 175503.
32 M. A. Zwijnenburg and S. T. Bromley, J. Mater. Chem., 2011, 21, 15255.
33 Y. Yong, B. Song and P. He, Phys. Chem. Chem. Phys., 2011, 13, 16182.
34 Y. Yong, B. Song and P. He, J. Phys. Chem. C, 2011, 115, 6455.
35 J. M. Matxain, L. A. Eriksson, E. Formoso, M. Piris and J. M. Ugalde, J. Phys. Chem. C, 2007, 111, 3560.
36 J. M. Matxain, M. Piris, X. Lopez and J. M. Ugalde, Chem.–Eur. J, 2009, 15, 5138.
37 E. Jimenez-Izal, J. M. Matxain, M. Piris and J. M. Ugalde, J. Phys. Chem. C, 2010, 114, 2476.
38 A. D. Becke, Phys. Rev. A, 1988, 38, 3098.
39 A. D. Becke, J. Chem. Phys., 1993, 98, 1372.
40 C. Lee, W. Yang and R. G. Parr, Phys. Rev. B: Condens. Matter, 1988, 37, 785.
41 W. Kohn and L. J. Sham, Phys. Rev., 1965, 140, A1133.
42 P. Hohenberg and W. Kohn, Phys. Rev., 1964, 136, B864.
43 W. J. Stevens, M. Krauss, H. Basch and P. G. Jasien, Can. J. Chem., 1992, 70, 612.
44 M. J. Frisch, G. W. Trucks, H. B. Schlegel, G. E. Scuseria, M. A. Robb, J. R. Cheeseman, G. Scalmani, V. Barone, B. Mennucci, G. A. Petersson, H. Nakatsuji, M. Caricato, X. Li, H. P. Hratchian, A. F. Izmaylov, J. Bloino, G. Zheng, J. L. Sonnenberg, M. Hada, M. Ehara, K. Toyota, R. Fukuda, J. Hasegawa, M. Ishida, T. Nakajima, Y. Honda, O. Kitao, H. Nakai, T. Vreven, J. A. Montgomery, Jr., J. E. Peralta, F. Ogliaro, M. Bearpark, J. J. Heyd, E. Brothers, K. N. Kudin,
V. N. Staroverov, R. Kobayashi, J. Normand, K. Raghavachari, A. Rendell, J. C. Burant, S. S. Iyengar, J. Tomasi, M. Cossi, N. Rega, J. M. Millam, M. Klene, J. E. Knox, J. B. Cross, V. Bakken, C. Adamo, J. Jaramillo, R. Gomperts, R. E. Stratmann, O. Yazyev, A. J. Austin, R. Cammi, C. Pomelli, J. W. Ochterski, R. L. Martin, K. Morokuma, V. G. Zakrzewski, G. A. Voth, P. Salvador, J. J. Dannenberg, S. Dapprich, A. D. Daniels, O. Farkas, J. B. Foresman, J. V. Ortiz, J. Cioslowski and D. J. Fox, Gaussian, Inc., Wallingford CT, 2009.
45 J. M. Soler, E. Artacho, J. D. Gale, A. Garcia, J. Junquera, P. Ordejon and D. Sanchez-Portal, J. Phys.: Condens. Matter, 2002, 14, 2745.
46 J. Perdew, K. Burke and M. Ernzerhof, Phys. Rev. Lett., 1996, 77, 3865.
47 B. Hammer, L. B. Hansen and J. K. Norskov, Phys. Rev. B: Condens. Matter, 1999, 59, 7413.
48 N. Troullier and J. L. Martins, Phys. Rev. B: Condens. Matter, 1991, 43, 1993.
49 L. Kleinman and D. M. Bylander, Phys. Rev. Lett., 1982, 48, 1425.
50 J. M. Matxain, L. A. Eriksson, J. M. Mercero, X. Lopez, M. Piris, J. M. Ugalde, J. Poater, E. Matito and M. Sola, J. Phys. Chem. C, 2007, 111, 13354.

51 F. Benkabou, H. Aourag and M. Certier, Mater. Chem. Phys., 2000, 66, 10.

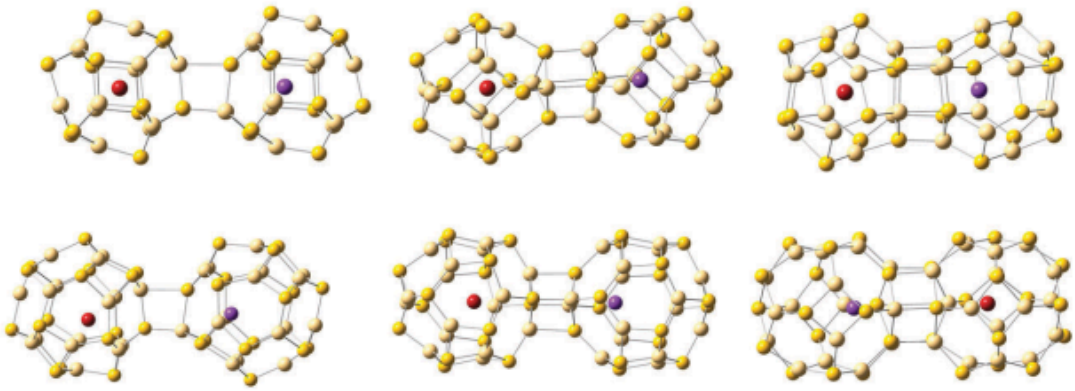

Fig. 1 Above K@$Cd_{12}S_{12}$–Br@$Cd_{12}S_{12}$ linked together by their edges, squares and hexagons, respectively are shown. Below K@$Cd_{16}S_{16}$–Br@$Cd_{16}S_{16}$ linked together by their edges, squares and hexagons, respectively, are shown. In violet K atom, in red Br atom, in dark yellow S atoms and light yellow Cd atoms, are depicted.

Dimer	R	q_K	q_X	Symm	E_{dim}	$\Delta\varepsilon_{HL}$
$Cd_{12}S_{12}$ (H–H)	8.77	—	—	S_6	−1.66	3.32
$Cd_{12}S_{12}$ (S–S)	9.82	—	—	C_{2V}	−1.26	3.43
$Cd_{12}S_{12}$ (E–E)	10.26	—	—	C_S	−0.92	3.45
K@$Cd_{12}S_{12}$–Cl@$Cd_{12}S_{12}$ (H–H)	7.75	0.49	−0.76	C_3	−4.44	2.74
K@$Cd_{12}S_{12}$–Br@$Cd_{12}S_{12}$ (H–H)	7.67	0.49	−0.78	C_3	−4.49	2.76
K@$Cd_{12}S_{12}$–Cl@$Cd_{12}S_{12}$ (S–S)	8.78	0.51	−0.79	C_1	−3.69	2.44
K@$Cd_{12}S_{12}$–Br@$Cd_{12}S_{12}$ (S–S)	8.86	0.51	−0.81	C_1	−3.71	2.42
K@$Cd_{12}S_{12}$–Cl@$Cd_{12}S_{12}$ (E–E)	9.65	0.52	−0.80	C_1	−2.94	2.00
K@$Cd_{12}S_{12}$–Br@$Cd_{12}S_{12}$ (E–E)	9.58	0.52	−0.82	C_1	−2.97	1.98
$Cd_{16}S_{16}$ (H–H)	10.34	—	—	C_{2H}	−1.65	3.25
$Cd_{16}S_{16}$ (S–S)	11.16	—	—	D_{2D}	−1.51	3.33
$Cd_{16}S_{16}$ (E–E)	11.48	—	—	C_{2H}	−0.76	3.31
K@$Cd_{16}S_{16}$–Cl@$Cd_{16}S_{16}$ (H–H)	8.14	0.51	−0.72	C_1	−4.69	2.65
K@$Cd_{16}S_{16}$–Br@$Cd_{16}S_{16}$ (H–H)	8.28	0.51	−0.73	C_S	−4.64	2.63
K@$Cd_{16}S_{16}$–Cl@$Cd_{16}S_{16}$ (S–S)	9.17	0.54	−0.73	C_S	−3.97	2.23
K@$Cd_{16}S_{16}$–Br@$Cd_{16}S_{16}$ (S–S)	9.19	0.54	−0.75	C_S	−3.95	2.26
K@$Cd_{16}S_{16}$–Cl@$Cd_{16}S_{16}$ (E–E)	9.44	0.51	−0.78	C_1	−3.09	2.29
K@$Cd_{16}S_{16}$–Br@$Cd_{16}S_{16}$ (E–E)	9.60	0.52	−0.78	C_1	−3.06	2.12

Table 1. Different bare and doped $Cd_{12}S_{12}$ and $Cd_{16}S_{16}$ built dimers. R is the distance between the center of mass of both monomers, in the case of bare dimers, and between the encapsulated potassium atom and the corresponding halogen atom, in the case of doped dimers, and is given in Å. q_K and q_X are the charges of potassium and halogen atoms, respectively, and Symm stands for the symmetry group of each structure. Finally, E dim is the dimerization energy, and DE_{HL} is the HOMO–LUMO energy gap, both given in eV.

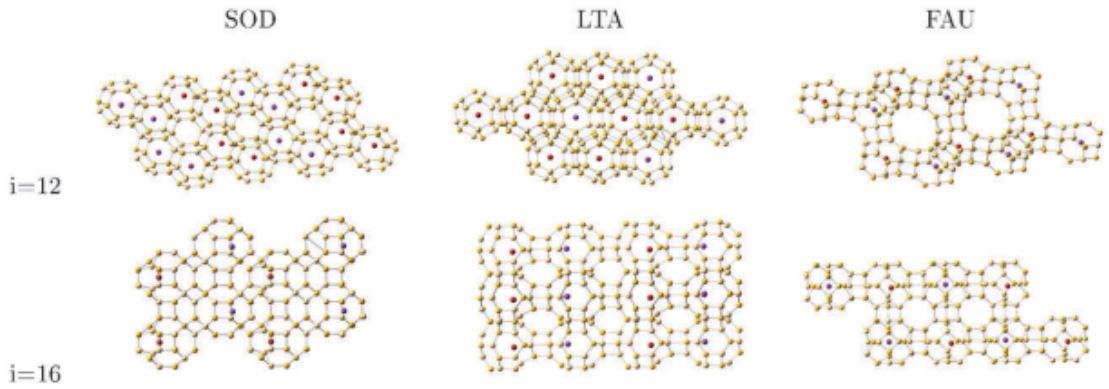

Fig. 2 Above, assembled SOD, LTA and FAU structures using K@$Cd_{12}S_{12}$–Br@$Cd_{12}S_{12}$ dimer as unit cell, and below SOD, LTA and FAU structures using K@$Cd_{16}S_{16}$–Br@$Cd_{16}S_{16}$ as unit cell are shown. In dark yellow S atoms, light yellow Cd atoms, violet K atom and in red Br atom are depicted.

Unit cell	*R*	*V*	*a*	*b*	*c*	E_{coh}	Δ_Γ
FAU-$Cd_{12}S_{12}$	9.26	2324.90	15.04			−1.13	1.67
LTA-$Cd_{12}S_{12}$	9.98	2028.18	14.38			−1.55	1.66
SOD-$Cd_{12}S_{12}$	10.80	1662.51	10.78	21.58		−1.63	1.31
FAU-K@$Cd_{12}S_{12}$–Cl@$Cd_{12}S_{12}$	8.95	2272.52	15.23			−1.65	1.63
FAU-K@$Cd_{12}S_{12}$–Br@$Cd_{12}S_{12}$	9.12	2325.56	15.18			−1.64	1.65
LTA-K@$Cd_{12}S_{12}$–Cl@$Cd_{12}S_{12}$	10.05	2031.61	14.41			−2.00	1.22
LTA-K@$Cd_{12}S_{12}$–Br@$Cd_{12}S_{12}$	10.04	2030.51	14.41			−2.02	1.33
SOD-K@$Cd_{12}S_{12}$–Cl@$Cd_{12}S_{12}$	10.62	1664.62	10.81	21.71		−2.42	1.22
SOD-K@$Cd_{12}S_{12}$–Br@$Cd_{12}S_{12}$	10.90	1661.02	10.77	21.57		−2.43	1.28
FAU-$Cd_{16}S_{16}$	10.86	2588.88	21.76	11.35	15.17	−1.48	1.56
LTA-$Cd_{16}S_{16}$	11.34	2912.21	11.32	22.71		−1.19	1.76
SOD-$Cd_{16}S_{16}$	12.23	2261.21	10.92	18.95		−1.69	1.21
FAU-K@$Cd_{16}S_{16}$–Cl@$Cd_{16}S_{16}$	11.12	2605.10	21.90	11.27	15.29	−2.01	1.52
FAU-K@$Cd_{16}S_{16}$–Br@$Cd_{16}S_{16}$	10.68	2605.73	21.89	11.27	15.34	−2.02	1.52
LTA-K@$Cd_{16}S_{16}$–Cl@$Cd_{16}S_{16}$	11.51	2944.10	11.31	23.01		−1.59	1.32
LTA-K@$Cd_{16}S_{16}$–Br@$Cd_{16}S_{16}$	11.46	2958.16	11.35	22.96		−1.64	1.43
SOD-K@$Cd_{16}S_{16}$–Cl@$Cd_{16}S_{16}$	12.21	2250.04	10.90	18.95		−1.98	0.05
SOD-K@$Cd_{16}S_{16}$–Br@$Cd_{16}S_{16}$	12.23	2270.40	10.96	18.89		−2.15	1.06

Table 2. Different solids from bare and doped $Cd_{12}S_{12}$ and $Cd_{16}S_{16}$ dimers. R is the distance between the center of mass of each monomer in the case of bare solids, and encapsulated potassium atom and the corresponding halogen atom (Å) for doped solids. V is the volume of the unit cell in $Å^3$. a, b and c are the lattice constants in Å, E_{coh} is the cohesive energy in eV, and the band gaps calculated at G point (DG in eV).

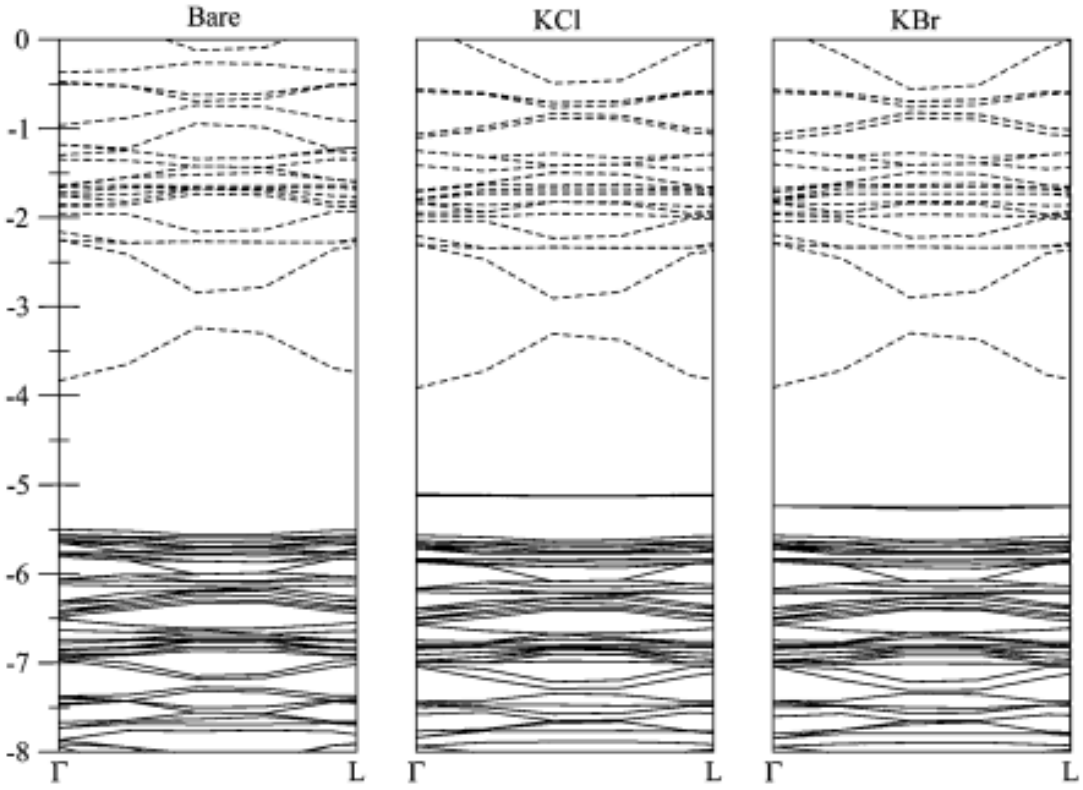

Fig. 3 Band structures of the calculated LTA $Cd_{12}S_{12}$, $K@Cd_{12}S_{12}$–$Cl@Cd_{12}S_{12}$ and $K@Cd_{12}S_{12}$–$Br@Cd_{12}S_{12}$ solids. The occupied bands are depicted with continuous lines and the unoccupied bands with dotted lines.

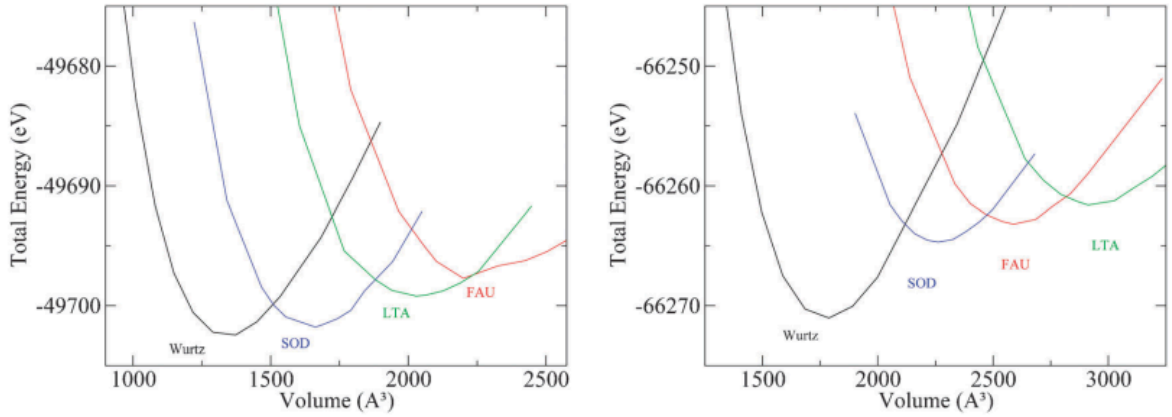

Fig. 4 Total energy as a function of cell volume for SOD, LTA and FAU phases of $Cd_{12}S_{12}$ (left) and $Cd_{16}S_{16}$ (right), compared with wurtzite structure.